Chapter 6

Dielectric studies on twist grain boundary phases

6.1 Introduction

Dielectric properties are related to the response of matter to the application of an external electric field [61, 62] (see section 1.10.3). Debye [63] demonstrated that the dielectric polarisation of the medium

$$\mathbf{P} = \epsilon_0(\epsilon^* - 1)\mathbf{E} \tag{6.1}$$

where E is the external electric field, ϵ_0 is the dielectric constant of vacuum and ϵ^* is the complex relative dielectric constant. The polarisation arises from the induced polarisation P_1 and the orientational polarisation P_2. P_1 consists of two parts: the electronic polarisation and the ionic polarisation. P_2 is connected with the partial orientation of the permanent molecular dipole moments in the direction of the external field.

Dielectric constants are frequency dependent as the dipoles take a finite time to respond to an alternating external electric field. When the frequency of the applied field becomes comparable with the reciprocal of the response time, it leads to dielectric relaxation (see section 1.11). The frequency dependence of the dielectric

constant gives information about the dynamic behaviour of the molecules in the system. The complex dielectric constant can be written as

$$\epsilon^* = \epsilon' - i\epsilon'' \tag{6.2}$$

where ϵ' is the real part of the dielectric constant. The imaginary part ϵ'' is a measure of the loss associated with the relaxation processes.

The dielectric anisotropy $\Delta\epsilon$ is given by

$$\Delta\epsilon = \epsilon_{\|} - \epsilon_{\perp}. \tag{6.3}$$

where $\epsilon_{\|}$ and $\epsilon_{\perp}$ are the principal dielectric constants parallel and perpendicular to the director respectively. For nematic liquid crystals consisting of polar molecules with strong dipoles along their long axes, $\Delta\epsilon$ usually has values between 10 to 20. Maier and Meier [64] have extended Onsager's theory for polar molecules [61] to the nematic state. They have related the macroscopic dielectric anisotropy with the anisotropies arising due to various molecular parameters. The assumptions of Maier and Meier are the following: a) the molecule has two principal polarisabilities α_l and α_t, along and transverse to the long axis, b) the molecule has a permanent dipole μ that makes an angle β with the long axis, and c) the molecule is in a spherical cavity with the surrounding medium being a continuum. By the aid of this simple model Maier and Meier arrived at the following expressions for $\epsilon_{\|}$, $\epsilon_{\perp}$ and $\Delta\epsilon$:

$$\epsilon_{\|} = 1 + 4\pi\frac{N_A\rho hF}{M}\left\{\bar{\alpha} + \frac{2}{3}\Delta\alpha S + \frac{F\mu^2}{3k_BT}\left[1 - \left(1 - 3\cos^2\beta\right)S\right]\right\} \tag{6.4}$$

$$\epsilon_{\perp} = 1 + 4\pi\frac{N_A\rho hF}{M}\left\{\bar{\alpha} - \frac{1}{3}\Delta\alpha S + \frac{F\mu^2}{3k_BT}\left[1 + \frac{1}{2}\left(1 - \cos^2\beta\right)S\right]\right\} \tag{6.5}$$

$$\Delta\epsilon = 4\pi\frac{N_A\rho hF}{M}\left[\Delta\alpha - F\left(\frac{\mu^2}{2k_BT}\right)(1 - 3\cos^2\beta)\right]S \tag{6.6}$$

where N_A is the Avogadro number, p is the density, M is the molecular weight, $h = 3\bar{\epsilon}/(2\bar{\epsilon}+1)$ is the cavity field factor $F = 1/(1-f\bar{\alpha})$ (where $f = (\bar{\epsilon}-1)/[2\pi a^3(2\bar{\epsilon}+1)]$

the reaction field factor for a spherical cavity [61]), $\mathbf{Aa} = \alpha_l - \alpha_t$ and $\bar{\epsilon}$ and $\bar{\alpha}$ are the average dielectric constant and polarisability respectively. Equations 6.4-6.6 account for many features of the anisotropic permittivity of nematics . It can be seen from Equation 6.6 that the contribution of the orientational polarisation to the dielectric anisotropy is positive when the angle made by the dipole moment with respect to the long axis of the molecule is $\leq 55°$ and is negative otherwise. If this negative quantity is larger than **Aa** then gives rise to a material with negative dielectric anisotropy.

The relaxation behaviour about $\epsilon_{||}$ and $\epsilon_{\perp}$ can provide information of the dynamic behaviour of the molecules in the liquid crystalline phase. In the case of a single relaxation over the whole temperature range of interest, the temperature dependence of the relaxation time can be represented as

$$\tau_r \propto exp\left(\frac{E_a}{k_B T}\right) \tag{6.7}$$

where E_a is denoted as the activation energy and k_B is the Boltzmann constant. The activation energy for the dielectric relaxation of $\epsilon_{||}$ in the liquid crystalline phases is a measure of both the rotational potential barrier against flipping of the molecule about the short axis and dissipation due to a relevant friction coefficient. When the magnitude of E_a becomes larger the probability for a molecule to flip diminishes.

$$\tau_r = \frac{1}{2\pi f_r} \tag{6.8}$$

where f_r is the relaxation frequency. Hence we get

$$lnf_r = \frac{-E_a}{k_B T} + C \tag{6.9}$$

where C is a constant. The variation of the natural logarithm of f_r with (1/T) is known as the Arrhenius plot. The slope of the line is equal to E_a/k_B, from which the activation energy can be calculated.

Nematic phase is not ferroelectric due to the apolar nature of the director n. Smectic C* is also referred to as a ferroelectric liquid crystal as mentioned in section 1.3.2. The chirality of the molecules removes the mirror plane from the symmetry group C_{2h} of the smectic C phase and the local point symmetry of the smectic C* layer is C_2. This lower symmetry of the smectic C* layers allows them to be transversely polarised along the C_2 axis. Due to the spontaneous polarisation of the ferroelectric liquid crystal there is a sharp increase in the dielectric constant at the smectic A to smectic C* transition.

In the ferroelectric phase, experiments have shown that two different collective modes, the Goldstone mode and soft mode can be observed depending on the alignment of smectic layers and their spatial director configuration. The Goldstone mode appears due to the phase fluctuations of the tilt angle of the molecules in the smectic C* phase while soft mode appears due to the fluctuations of the amplitude of tilt angle. For Goldstone mode the relaxation frequency is of the order of a few Hz-KHz which is practically independent of temperature. On the other hand the soft mode relaxation frequency is around 1MHz and decreases to zero as smectic C*-smectic A transition temperature is approached.

Over the last ten years, several compounds having chiral molecules have been found to exhibit new liquid crystalline phases called twist grain boundary phases [65]. In the TGB_A phase (see Fig. 1.5 (a)), slabs of almost perfect smectic A layers are regularly stacked in a helical fashion along an axis parallel to the smectic layers. Adjacent slabs are continuously connected via a grain boundary which consists of a grid of parallel equispaced screw dislocation lines. Subsequently a TGB_C phase was discovered where the slabs are of smectic C type [66] (see Fig. 1.5 (b)). Recently a new TGB phase namely $UTGB_{C^*}$ phase was discovered [5] (as described in section 1.4). In the $UTGB_{C^*}$ phase the tilted molecules are arranged in a helical fashion

within the smectic C* slabs. These slabs exhibit a 2D undulation in the form of a square lattice. In the case of a cell treated for homogeneous alignment, the slabs have an helical arrangement whose axis is normal to the glass plates and a square grid pattern is observed. When the glass plates are treated for homeotropic alignment an undulatory filament texture is observed in thin cells. Each filament corresponds to a rotation of the director by π radians, and the width of the filament $\approx p/2$, where p is the pitch of the TGB helix.

Dielectric studies on TGB phases are very rare [67, 68]. The measurements on the TGB_A phase [67] show that the dielectric behaviour at the smectic C*-TGB_A transition is similar to that at the smectic C*-smectic **A** transition. The dielectric properties of a compound having both TGB_A and TGB_C have been studied by Bougrioua etal [68]. They have attributed the observed two relaxation processes to soft mode and Goldstone mode in the TGB_C phase. These two modes are detected with lower amplitudes and higher frequencies (especially the Goldstone mode) compared to those in the smectic C* phase. They have explained qualitatively the experimental results on TGB phases using a model in which the structure of the liquid crystal is taken into account. The low amplitudes of the soft mode and the Goldstone mode are explained by elastic distortions within the blocks and these distortions depend on the block size. In the smectic C* phase, the restoring torque of the Goldstone mode is determined by the twist elasticity of the system. The restoring torque is proportional to $K_{22}q_o^2$, where K_{22} is the twist elastic constant. The wave vector $q_o=2\pi/p$ where p is the helical pitch in the smectic C* phase. In the case of TGB liquid crystals, Bougrioua etal have assumed strong anchoring of the director at the boundaries of the blocks. Hence in the TGB_A phase, an electric field applied perpendicular to the helical axis gives an electroclinic effect, and induces a director tilt which is larger in the center of the block than at the boundaries. In the

TGB_C phase, when an electric field is applied parallel to the helical axis, the field component in the smectic layers induces a rotation of the director around the cone. As strong anchoring is assumed at the boundaries of the blocks, the Goldstone mode is balanced by elastic torques due to twist deformations within the blocks. Hence they introduced a term H_2 in place of the normal twist energy term $K_{22}q_o^2$ in the amplitude of the relevant relaxation process, where H_2 is proportional to K_{22}/L_b^2 and L_b is the block length. The H_2 term is strongly dependent on the helical pitch p of the TGB helix and the block length. At the TGB_A-TGB_C transition H_2 remains important when the block length and pitch have small values. The very high frequency observed for soft mode at the TGB_A-TGB_C transition and for the Goldstone mode in the TGB_C phase compared to the smectic C* phase is attributed to the H_2 term.

The main results described in this chapter are on a binary mixture which exhibits a new TGB phase namely $UTGB_C^*$ phase (as mentioned above), in addition to the usual TGB_A and cholesteric phases.

6.2 Measurement geometries

In order to measure $\epsilon_{||}$ or $\epsilon_{\perp}$ the electric field applied should be parallel or perpendicular to the director. In the case of nematic and smectic A $\epsilon_{||}$ is obtained using a cell with homeotropic alignment and $\epsilon_{\perp}$ in a cell with homogeneous alignment.

In the case of cholesteric liquid crystals for a homogeneously aligned cell we measure the dielectric constant along the helix axis h. Hence [21]

$$\epsilon_{||h} = \epsilon_{\perp} \qquad \textit{(6.10)}$$

In the case of a homeotropically aligned cholesteric liquid crystalline sample we

measure the dielectric constant perpendicular to the helix axis. Hence

$$\epsilon_{\perp h} = \frac{1}{2}(\epsilon_{\parallel} + \epsilon_{\perp}) \tag{6.11}$$

For smectic C* liquid crystals in the case of a homogeneously aligned cell we measure the dielectric constant perpendicular to the helix axis.

$$\epsilon_{\perp h} = \frac{1}{2}\epsilon_{\perp}(1 + \cos^2\theta) + \epsilon_{\parallel}\sin^2\theta \tag{6.12}$$

where θ is the tilt angle [69]. For a homeotropically aligned cell, the smectic layers are parallel to the glass plates, and

$$\epsilon_{\parallel h} = \epsilon_{\parallel}\cos^2\theta + \epsilon_{\perp}\sin^2\theta \tag{6.13}$$

6.3 Experimental setup

The experimental setup is designed to go upto very high frequencies (500 MHz) even though our measurements are limited to 1MHz frequency range. In the high frequency regime the losses due to test leads become very high. Hence for dielectric measurements in the high frequency regime special provisions are required in the heater assembly. We built a heater assembly which can be used for high frequency (upto 500MHz) measurements.

The schematic diagram of the experimental setup is shown in Fig. 6.1. The heater dimensions are 4.3cms x 3.2cms x 1.6cms which are fixed so that the heater can be placed between two pole pieces of an electromagnet(Bruker magnet). A maximum magnetic field of 2.5 Tesla can be applied to the sample. The heater can be rotated by 90^o so that by using the magnetic field the parallel and perpendicular components of dielectric constant can be measured using the same cell. The impedance analysers HP4191A and HP4192A are used for the capacitance measurements.

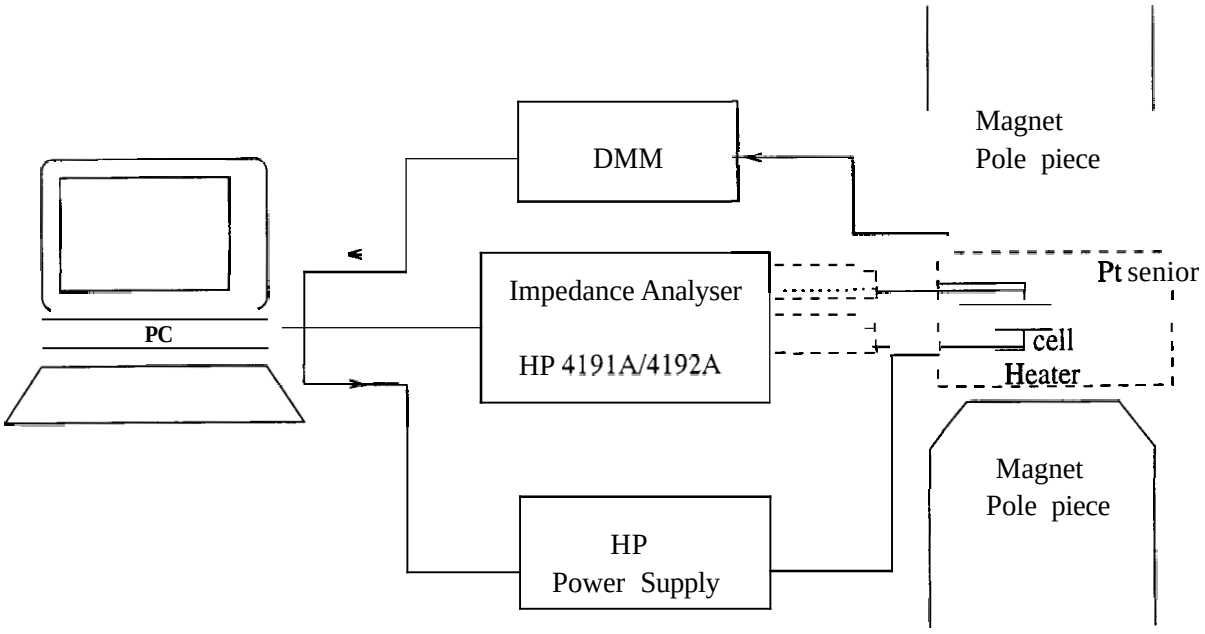

Fig. 6.1: Block diagram of the experimental setup for dielectric measurements. The dotted line shows the connection from the cell electrodes to the semirigid cable connected to HP4191A and the dashed lines from the cell electrodes show the connection to the four probe connector from HP4192A.

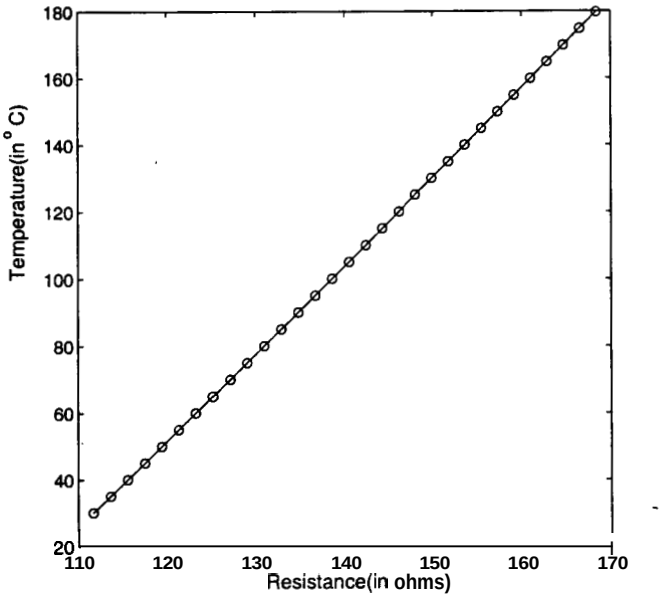

Fig. 6.2: Temperature calibration curve for the platinum resistance thermometer with respect to a factory calibrated Minco platinum resistance thermometer.

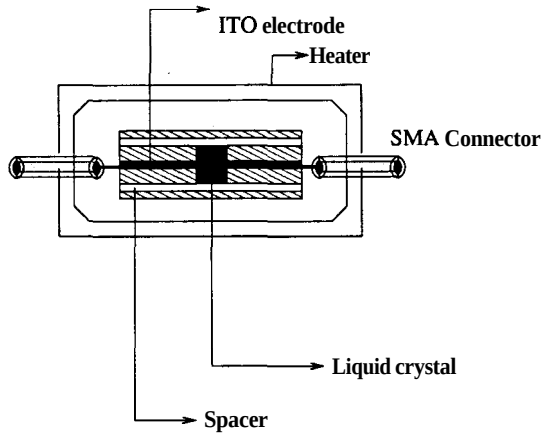

Fig. 6.3: The cross section of the cell used for dielectric measurements.

The heating element(Minco Kapton Foils) is connected to a HP programmable power supply($\pm$ 60V). The resistance of the heating element is 52.5Ω. A Minco platinum resistance thermometer is used for measuring the temperature of the sample. To measure the resistance R of the platinum resistor, it is connected to a Keithley 193A digital multimeter through a four probe connection. The platinum resistor is calibrated(see Fig. 6.2) by fixing it close to a factory calibrated resistance thermometer. The calibration curve is fitted to a second order polynomial and the temperature of the platinum resistance thermometer T_p is given by

$$T_p = -244.06620772 + 2.3312892142 * R + 0.0011016235 * R * R. \qquad (6.14)$$

The heater assembly with the cell used for dielectric measurements is shown in Fig. 6.3. The cell (Fig. 6.3) is made of two ITO coated transparent electrodes. A rectangular pattern with extensions for electrical connections, is etched on the ITO plates by using dilute hydrochloric acid and zinc dust. The cell is a parallel plate capacitor made of two such conducting ITO electrodes. The advantage of using ITO coated cells is that alignment can be checked under a microscope. But beyond 200KHz the impedance of the ITO layers is no longer negligible and it starts

contributing to the measured dielectric loss. The top and bottom electrodes are separated by mylar spacers of appropriate thickness placed in the etched portion so that the mylar spacers do not interfere with dielectric measurements of the liquid crystal. The electrodes are soldered on to the Sub Miniature Amphenol (SMA) connectors embedded in the heater.

Semi rigid cables are used for making connections from the impedance analyser HP4192A to reduce losses due to cables and these losses become more prominent in the high frequency regime. Due to the metal shielding of the semirigid cables they have more noise immunity compared to the BNC cables. The SMA connectors are connected to the impedance analyser HP4192A through a four probe configuration as shown in Fig 6.1. This configuration is used to eliminate errors due to residual impedance of test leads. The terminals consist of four connections: high current, high voltage, low current and low voltage. The current terminals are used to drive a signal current through the sample. The potential terminals are for detecting the voltage drop across the sample. High current and high voltage, are connected together and also the low current and low voltage terminals are connected together. In addition the shields of all conductors must be connected together. The capacitance measuring range is 0.0001 nF to 100 mF and the frequency range is 5Hz to 13MHz. However we found that our impedance analyser gave accurate results only in the 1KHz-1MHz frequency range. We have interfaced the whole experimental setup using a Keithley card and C language to a PC. An AC signal is applied across the sample using 4192A and the capacitance measurement is based on an impedance analysis of the amplitude and phase of the output AC signal from'the sample.

The liquid crystal is filled by capillary action in the central rectangular region of the ITO coated glass plates. The heater is calibrated using known samples. The dielectric constant is measured for these known samples as a function of tempera-

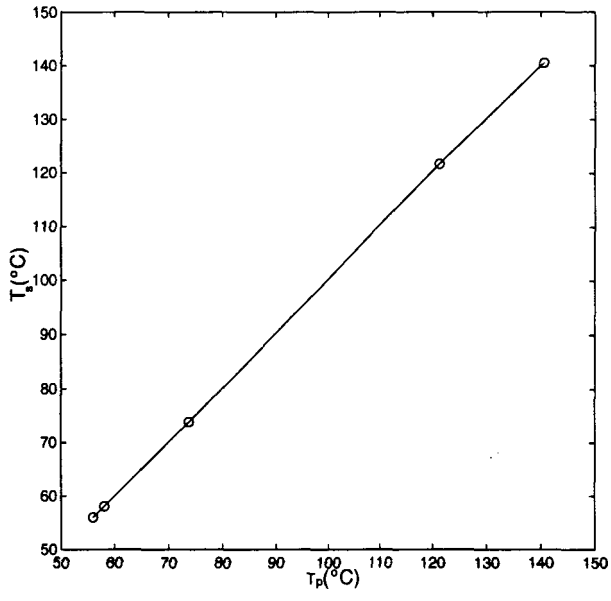

Fig. 6.4: Temperature calibration curve for the sample temperature(T_s) with respect to the temperature measured by platinum resistance thermometer(T_p).

ture measured by the platinum resistor(T_p). The transition temperatures of various liquid crystalline phases measured by the platinum resistor for these samples are obtained using the dielectric data. These temperatures are compared with the known transition temperatures of these samples. It is found that the temperature near the sample is in good agreement with T_p(see Fig. 6.4) .

6.4 Dielectric measurements using LIA

As mentioned above, the impedance analyser gave accurate data only above 1KHz. A lock-in amplifier has been used for the dielectric measurements around 1KHz. We measure the impedance of the sample cell and calculate its-capacitance and resistance. As described in Section **3.3** the equivalent electrical circuit of a liquid crystal cell can be considered to be a capacitance (C_s) and a resistance (R_s) in parallel. The experimental setup to measure C_s and R, of a liquid crystal cell is

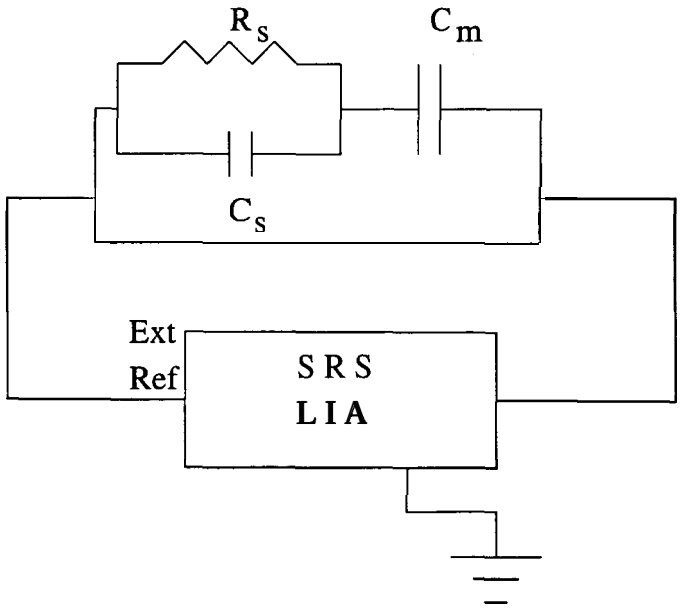

Fig. 6.5: Block diagram of the experimental setup to measure capacitance and resistance of a liquid crystal cell.

shown in Fig. 6.5. We measure the amplitude and phase of the voltage developed across a series capacitance, C_m (~ 1 μFarad), which is large in comparison to the capacitance of the sample cell (~ 150 pF). It is important that C_m is large so that the maximum voltage drop is across the cell and only a small voltage is measured by the LIA. The impedance of the sample cell is given by

$$Z_c = R_s \frac{(1 - i\omega C_s R_s)}{1 + \omega^2 C_s^2 R_s^2} \tag{6.15}$$

where R_s is the resistance and C_s is the capacitance of the cell. $w = 2\pi \mathrm{f}$ where f is the frequency of the applied voltage (V_o) across the cell. The total impedance of the circuit (Z_t) is given by

$$Z_t = \frac{\omega R_s C_m - i(1 + \omega^2 R_s^2 C_s (C_m + C_s))}{\omega C_m (1 + \omega^2 C_s^2 R_s^2)} \tag{6.16}$$

The total current I_t, is given by

$$I_t = \frac{V_o e^{i(\omega t)} \omega C_m (1 + \omega^2 C_s^2 R_s^2))}{\omega R_s C_m - i(1 + \omega^2 R_s^2 C_s (C_m + C_s))} \tag{6.17}$$

The voltage drop across C_m which is measured by the LIA is given by

$$V = V_m e^{i(\omega t + \phi_m)} = I_t Z_3 \tag{6.18}$$

where $Z_3 = 1/(i\omega C_m)$ and V_m and ϕ_m are the amplitude and phase of the measured voltage.

$$V_m = |V| \tag{6.19}$$

$$\tan \phi_m = \frac{ImV}{ReV} \tag{6.20}$$

Simplifying the above expressions it can be shown that the sample resistance (R,) and capacitance (C_s) are given by:

$$R_s = Y/2\pi \mathrm{f} \sin a \tag{6.21}$$

$$C_s = X/Y \tag{6.22}$$

where $X = \cos\alpha - \mathrm{Q}$, $\mathrm{Y} = (\sin^2\alpha + X^2)/C_m Q$, $\mathrm{Q} = V_m/V_o$ and $a = -\phi_m$. The dielectric constant of the sample is given by the ratio C_s/C_o where C_o is the capacitance of the empty cell measured before filling it. We used a standard capacitor and resistor connected in parallel in place of the sample cell to measure the stray capacitance added to the circuit by the cables used. It was found to be ~ 4 pF. The absolute accuracy of the measured capacitance is 1 to 2% whereas that of the resistance is $\sim 8\%$.

6.5 Results

The dielectric measurements have been performed on binary mixtures of the chiral compound 4-(2'- methyl butyl phenyl 4′-n-octylbiphenyl-4-carboxylated (CE8)) and 2-cyano-4-heptyl-phenyl-4′-pentyl-4-biphenyl carboxylate (7(CN)5). The structures of the compounds CE8 and (7(CN)5) are shown in Fig. 6.6. CE8 exhibits the phase

CE8

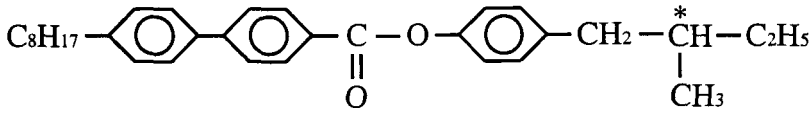

7CN5

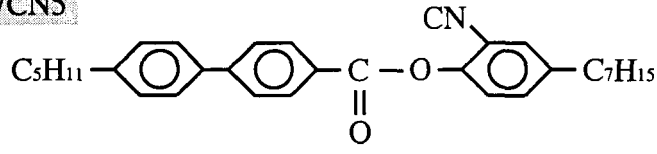

Fig. 6.6: The structures of the compounds CE8 and (7(CN)5).

sequence (with temperature in ^oC): crystal 67 S_{I^*} 70 S_{C^*} 85 S_A 134.6 N* 140.5 I, where N* stands for chiral nematic and I for isotropic phases. 7(CN)5 exhibits the phase sequence: crystal 45 N 102 I. The mixtures of these two compounds in a specific composition range exhibit a new TGB phase. Experiments were conducted on one such mixture with 36 wt % of 7(CN)5 exhibiting the following sequence of known phases while cooling: 121.7 N* 76.8 TGB_A. As the binary mixture is cooled to $\sim 60^oC$ it exhibits a transition to the new TGB phase namely $UTGB_{C^*}$ phase as mentioned in the beginning of this chapter. The dielectric studies were undertaken in cells treated for both homeotropic and homogeneous alignments. In these experiments we have used ITO coated glass plates treated with polyimide and rubbed for homogeneous alignment and plates treated with long ODSE molecules for homeotropic alignment. The thicknesses of the cells have been measured using channel spectrum (see section 1.12). The dielectric data given in this chapter are for cells of thicknesses $\sim 5.4\mu m$ for homeotropic alignment and $\sim 5.8\mu m$ for homogeneous alignment respectively. The measurements have been made as functions of temperature at various frequencies. Above 1KHz the experiments have been conducted using HP impedance analyser 4192A while at frequencies around 1KHz the lock-in amplifier was used. We did not perform the measurements in some of the

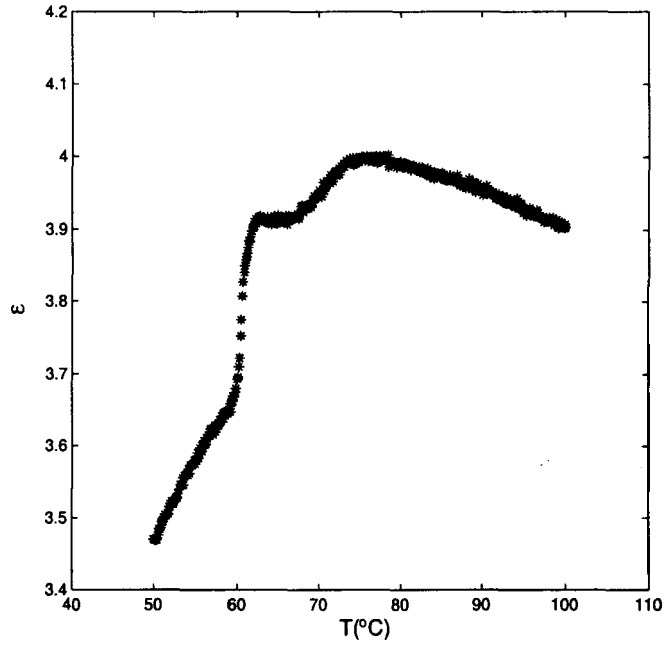

Fig. 6.7: Dielectric constant at 15KHz as a function of temperature for a cell treated for homeotropic alignment.

---

cases above $\sim 80^{o}$C as the mixture decomposes if it is heated to very high temperatures. In the case of homogeneous alignment the measurements were made in both heating mode as well as in cooling mode. The dielectric data were similar in both the cases. We present data collected in the cooling mode. In the homeotropic alignment case the measurements were made only in the heating mode as the alignment was not found to be good in the cooling mode. The temperature in which the UTGB_C^* phase occurs depends on the exact composition of the chiral and nonchiral components of the mixture. The phase transition from the TGB_A phase to the UTGB_C^* phase is clearly seen at $\sim 62^{o}$C in homeotropically aligned cell and at -60°C in homogeneously aligned cell(see Fig. 6.7-6.11). These figures are shown in the same order in which the experiments were performed.

In the homeotropic geometry the measurement at 15KHz was done using the impedance analyser immediately after filling the sample. The alignment was checked

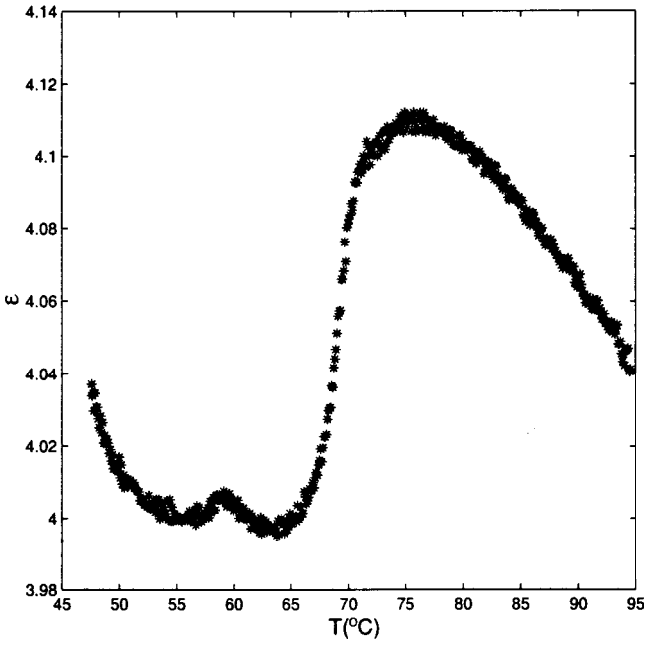

Fig. 6.8: Dielectric constant at 1KHz as a function of temperature for a cell treated for homeotropic alignment.

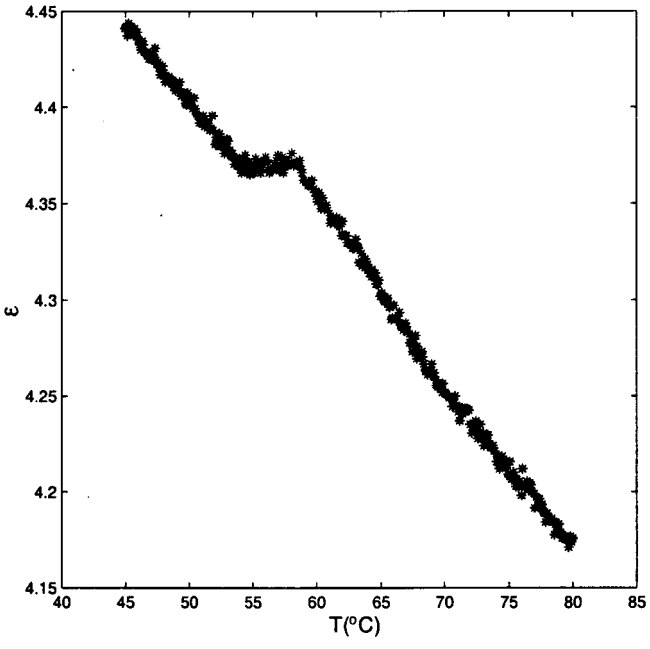

Fig. 6.9: Dielectric constant at 15KHz as a function of temperature for a cell treated for homogeneous alignment.

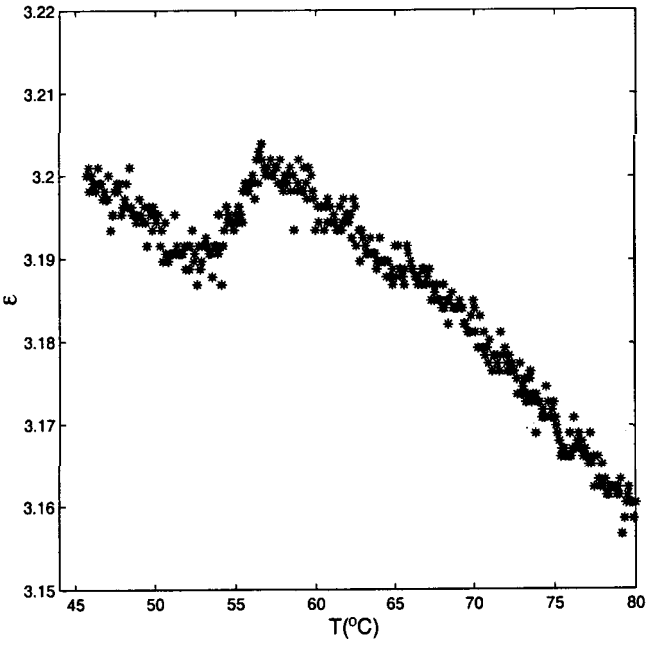

Fig. 6.10: Dielectric constant at 224KHz as a function of temperature for a cell treated for homogeneous alignment.

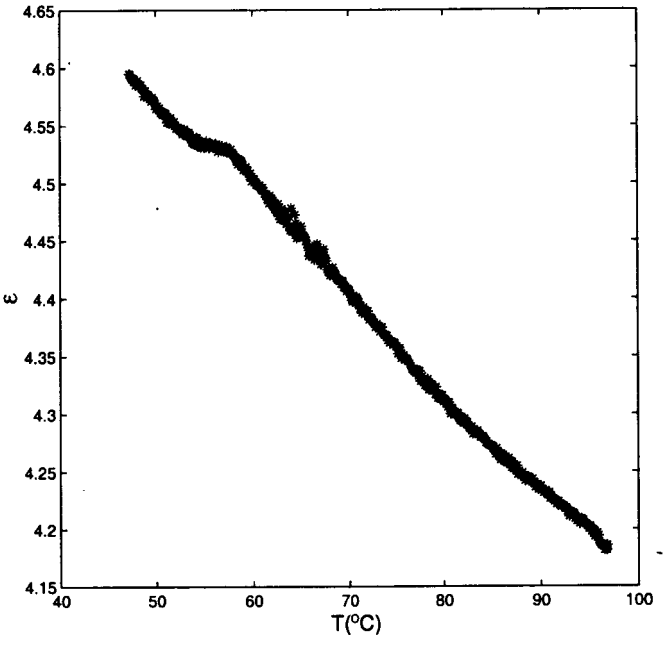

Fig. 6.11: Dielectric constant at 1KHz as a function of temperature for a cell treated for homogeneous alignment.

under a polarising microscope and was found to be good. The same homeotropically aligned cell was transferred later to the lock-in amplifier setup. The alignment had slightly deteriorated and some misaligned patches had developed in small regions. This cell was used for the measurement at lKHz in the lock-in amplifier setup.

In the homogeneous geometry the measurements at 15KHz and 224KHz were done using the impedance analyser. The cell was later transferred to the lock-in amplifier setup. for measuring the dielectric data at 1KHz. The alignment was found to be good in all the three measurements.

The temperature dependence of $\Delta\epsilon$ is mainly governed by that of the orientational order parameter S in the cholesteric phase. In the smectic C* phase, in addition to the orientational order parameter, the tilt angle(θ) also varies with temperature which also affects the temperature dependence of $\Delta\epsilon$.

The order parameter S is approximately related to the dielectric anisotropy by

$$S \approx \frac{\Delta\epsilon}{\Delta\epsilon_o} \tag{6.23}$$

where $\Delta\epsilon_o$ is the dielectric anisotropy for the fully aligned state. As $\Delta\epsilon = \epsilon_{||} - \epsilon_{\perp}$ and the average dielectric constant $\bar{\epsilon} = (\epsilon_{||} + 2\epsilon_{\perp})/3$ we get

$$\epsilon_{||} \approx \bar{\epsilon} + \frac{2}{3}\Delta\epsilon_o S \tag{6.24}$$

and

$$\epsilon_{\perp} \approx \bar{\epsilon} - \frac{1}{3}\Delta\epsilon_o S \tag{6.25}$$

In the cholesteric phase the dielectric constant measured using polyimide coated plates $\epsilon_{||h}$ is equal to $\epsilon_{\perp}$ (see equation 6.10). Similarly the dielectric constant measured using ODSE coated plates $\epsilon_{\perp h}$ can be related to $\epsilon_{||}$ and $\epsilon_{\perp}$ using equation 6.11. The calculated values of $\epsilon_{||}$ and $\epsilon_{\perp}$ at lKHz and 15Khz are shown in Fig. 6.12 and 6.13. $\Delta\epsilon$ is negative and small(—-0.4). Note that the values of $\epsilon_{||}$ and $\epsilon_{\perp}$ at lKHz

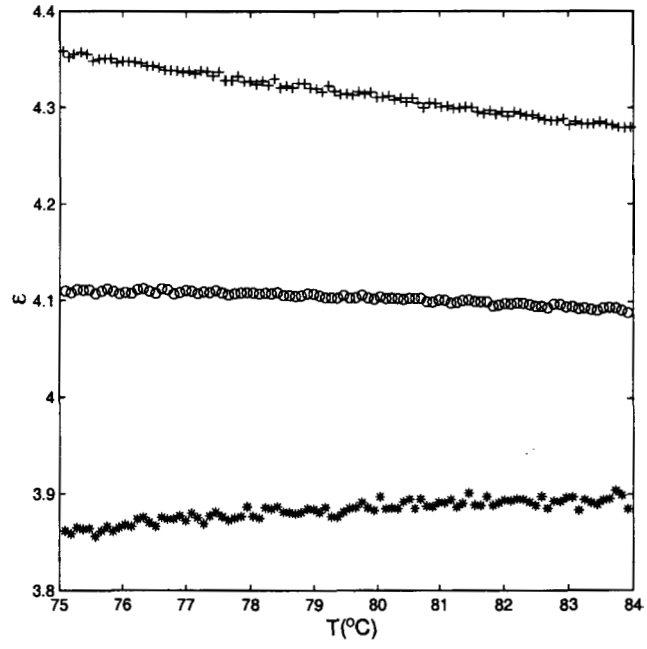

Fig. 6.12: The temperature dependence of the dielectric constant at 1KHz in the cholesteric phase of the binary mixture of CE8 and 7(CN)5. The '+' symbol stands for $\epsilon_{\|h}=\epsilon_{\perp}$, 'o' for $\epsilon_{\perp h}$ and '*' for $\epsilon_{\|}$ respectively.

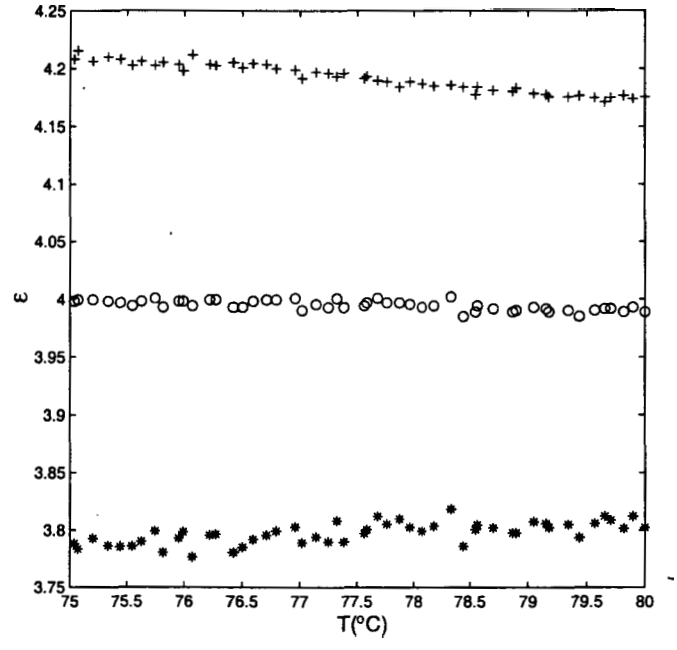

Fig. 6.13: The temperature dependence of the dielectric constant at 15KHz in the cholesteric phase of the binary mixture of CE8 and 7(CN)5. The '+' symbol stands for $\epsilon_{\|h}=\epsilon_{\perp}$, 'o' for $\epsilon_{\perp h}$ and '*' for $\epsilon_{\|}$ respectively.

are slightly higher (2-3%) than those at 15KHz. As these measurements were made using different instruments the difference in the values fall within the accuracies of these instruments. From equation 6.25 we can see that $\epsilon_\perp$ should increase as the temperature is decreased for a negative dielectric anisotropy material as can be seen in Fig. 6.12 and 6.13. This is due to the increase of S with decrease of temperature. Similarly $\epsilon_{||}$ should decrease as temperature is decreased for a negative dielectric anisotropy material (see equation 6.24) as seen in Fig. 6.12 and 6.13. However as we are far away from the cholesteric-isotropic transition point ($\sim 121^oC$), the temperature dependences of the order parameter and hence those of the dielectric constants $\epsilon_{||}$ and $\epsilon_\perp$ are not very strong.

For the sake of convenience we will discuss the results in the smectic C* phase before discussing the results in the TGB_A and $UTGB_{C*}$ phases. The smectic C* phase occurs below 58^oC in the case of homeotropically aligned cell and below 56^oC for homogeneously aligned cell. In the smectic C* phase the dielectric constant measured in both the geometries can be related to $\epsilon_{||}$ and $\epsilon_\perp$ using equations 6.12 and 6.13. The tilt angle(θ) variation with temperature governs the temperature dependence of $\Delta\epsilon$ in the smectic C* phase in addition to the orientational order parameter dependence. For small tilt angle $\epsilon_{||}$ contributes more than $\epsilon_\perp$ in the homeotropic geometry and vice versa in the case of homogeneous geometry as can be seen from equations 6.12 and 6.13. The tilt angle increases with decrease of temperature (see Fig. 6.14). This will result in an increase in the dielectric constant with decrease of temperature for a homeotropically aligned sample. However as discussed above the temperature variation of the orientational order parameter will result in a decrease in $\epsilon_{||}$. This in turn can decrease the dielectric constant in this geometry. There will be a net increase or decrease in the dielectric constant, depending on which of these processes will dominate. The dielectric constant at

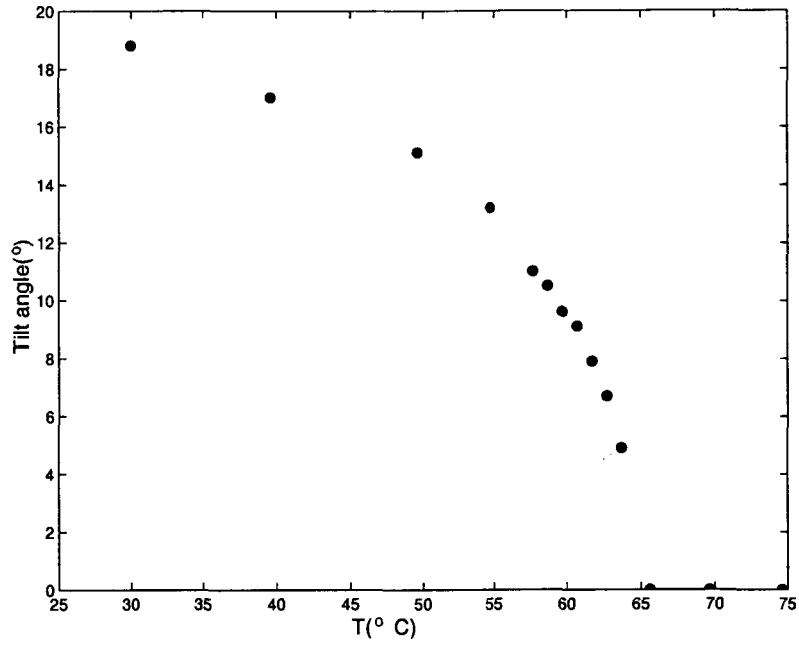

Fig. 6.14: The tilt angle variation with temperature in the $UTGB_{C*}$ phase and the smectic C* phase of the binary mixture of CE8 and 7(CN)5 (Courtesy P. A. Pramod).

1KHz in Fig. 6.8 increases with decrease of temperature. The increase is $\sim 0.2\%$ for a temperature range of 8^o in the smectic C* phase.

In this (homeotropic) geometry the temperature variations of the dielectric constant at 1KHz and 15KHz show different trends in the smectic C* phase. If the frequencies at which the measurements are made are comparable to the relaxation frequency then in addition to the tilt angle(θ) variation and the temperature variation of the orientational order parameter, the relaxation process also governs the temperature dependence of ϵ. The dielectric measurements shown in Fig. 6.15 and 6.16 were performed as functions of frequency at different temperatures. In Fig. 6.15 we see a relaxation in ϵ in the homeotropic geometry. We postpone the detailed discussion of the origin of the relaxation process to a later stage. Usually the relaxation frequency is identified from the peak in the imaginary part of the

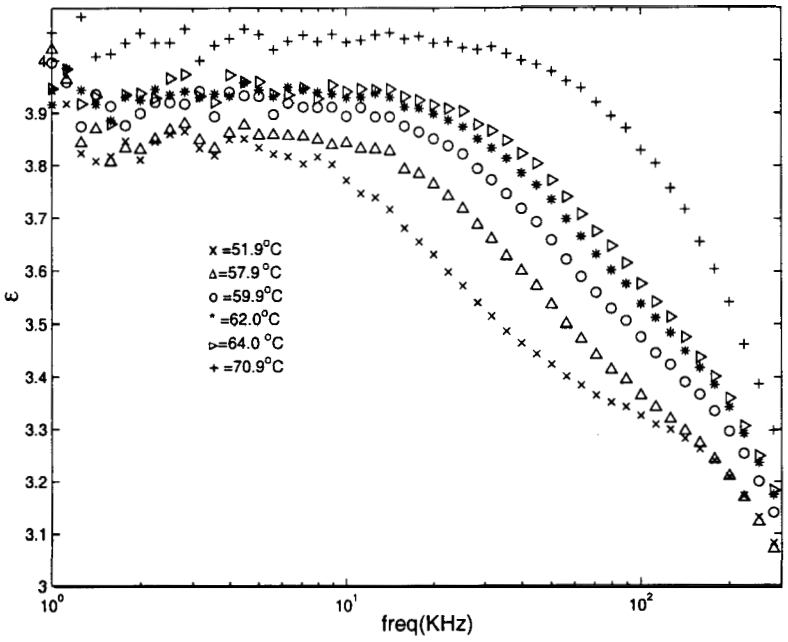

Fig. 6.15: Real part of the dielectric constant as a function of frequency for a cell treated for homeotropic alignment.

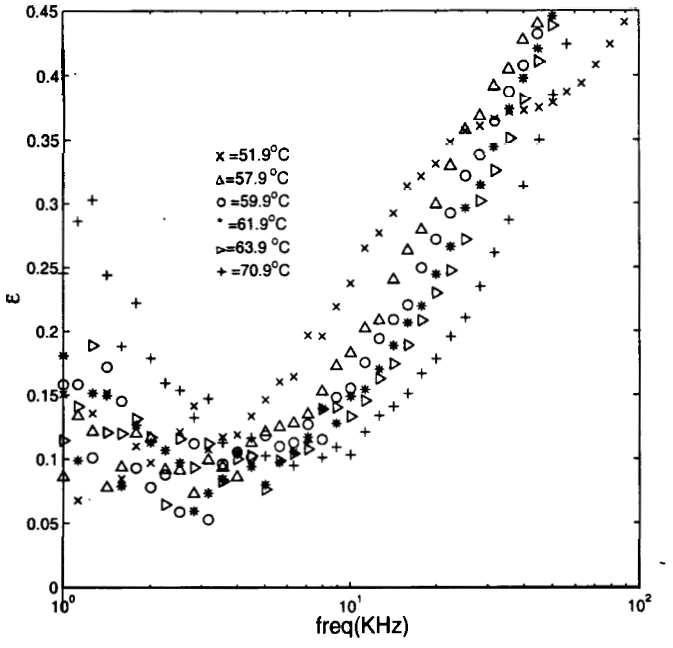

Fig. 6.16: Imaginary part of the dielectric constant as a function of frequency for a cell treated for homeotropic alignment.

dielectric constant. However we do not see any well defined peak (see Fig. 6.16) as the contribution from ITO layers becomes significant around 200KHz. However, in the real part of the dielectric constant a sharp change in slope occurs at a temperature dependent frequency. This frequency f_d is related to the relaxation frequency, and will be used in further discussion. In the imaginary part we see a small shoulder only at low temperatures and it is around 20KHz at $\sim 52^o$C(Fig. 6·16), while f_d is $\sim$10KHz. The measurements shown in Fig. 6.7 were performed at 15KHz. The dielectric constant decreases by —5% when the temperature decreases by 8^o in the smectic C* phase. This decrease in the dielectric constant at 15KHz indicates that the relaxation process dominates the temperature variation of the dielectric constant.

For estimating the contribution from the orientational order parameter to the dielectric constant in the smectic C* phase we now extrapolate the values of $\epsilon_{||}$ and $\epsilon_{\perp}$ in the cholesteric phase shown in Fig. 6.12 and 6.13 to lower temperatures. In order to take into account the tilt angle variation, we calculate the temperature variations of $\epsilon_{||h}$ and $\epsilon_{\perp h}$ from equations 6.12 and 6.13. As mentioned above the temperature at which the TGB_A to $UTGB_{C^*}$ phase transition occurs, depends on the exact composition of the chiral and nonchiral components of the mixture. In order to use the same tilt angles we have used the relative temperature T_c-T to perform the calculations where T_c is the measured transition temperature. The calculated temperature variations of $\epsilon_{||h}$ and $\epsilon_{\perp h}$ at 1KHz and 15KHz for both the geometries are shown in Fig. 6.17. As mentioned before the values of $\epsilon_{||}$ and $\epsilon_{\perp}$ in the cholesteric phase at 1KHz are higher than those at 15KHz. 'The same trend is seen in Fig. 6.17. The calculated values show a slight increase in the dielectric constant in the homeotropic geometry with decrease of temperature at 1KHz. The increase is —0.2% for a temperature range of 8^o in the smectic C* phase which is

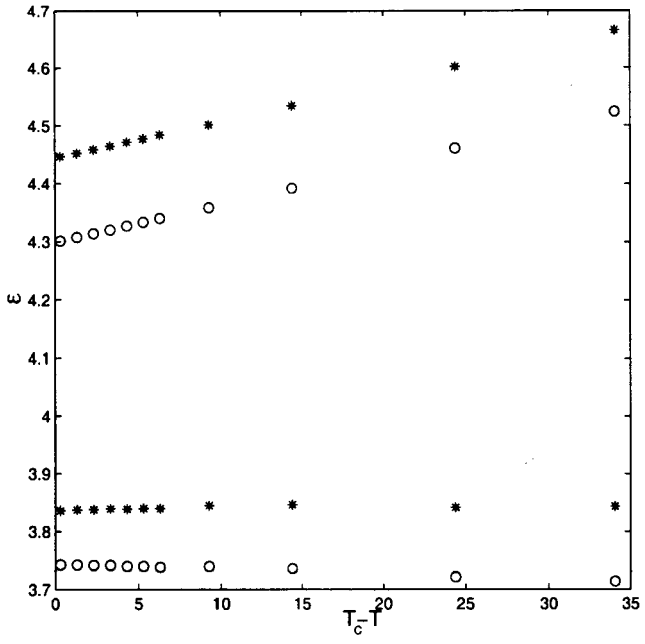

Fig. 6.17: The calculated temperature variations of $\epsilon_{\|h}$(lower two curves) and $\epsilon_{\perp h}$(upper two curves). '*' stands for data at 1KHz while 'o' stands for data at 15Khz.

similar to the increase observed experimentally. The calculated dielectric constant decreases by -0.1% for the same temperature range at 15KHz. The much larger decrease (-5%) observed experimentally is due to the relaxation of $\epsilon_{\|}$ taking place around this frequency (see Fig. 6.15) in the smectic C* phase.

In the homogeneous geometry the dielectric constant in the smectic C* phase increases with decrease of temperature. We see an increase in the dielectric constant of $\sim 1.1\%$ at 15KHz and -1.3% at 1KHz for a temperature range of 8^o. The calculated variations of $\epsilon_{\perp h}$ shown in Fig. 6.17 show an increase of -1.7% at 15KHz and $\sim 1.6\%$ at 1KHz, roughly agreeing with the experimental variations. The tilt angle variation will result in a decrease in the dielectric constant with decrease of temperature. The orientational order parameter variation with temperature will give rise to an increase in $\epsilon_{\perp}$ which in turn will increase the dielectric constant in

this geometry. The measured as well as calculated increase in the dielectric constant indicates that the orientational order parameter variation dominates rather than the tilt angle variation.

In the TGB_A phase in the homogeneous geometry the texture is very similar to that in the cholesteric phase. We do not see any distinct transition to the TGB_A phase using dielectric measurements in the homogeneous geometry. The dielectric constant increases smoothly with decreasing temperature(see Fig. 6.9). This is due to the temperature variation of the order parameter as seen in the cholesteric phase. The transition to the TGB_A phase is clearly seen in Fig. 6.7 and 6.8 in the homeotropic geometry at $\sim 74^o$C. In this geometry, in some parts of the cell, filaments are seen in the TGB_A phase. Each filament corresponds to a rotation of the director by π radians. The relative contributions from $\epsilon_{||}$ and $\epsilon_{\perp}$ depend on the number of filaments and the alignment of the director within the filaments. These filaments are like fingerprint texture in the cholesteric phase though on a smaller scale, especially for thin cells($\sim 5\mu m$). In addition to the filaments in the TGB_A phase, we have homeotropically aligned, unwound TGB_A domains (which hence mimic smectic A domains). These domains grow with decreasing temperature and hence the contribution of $\epsilon_{||}$ increases. If we assume a filamentary texture throughout the sample equations 6.10 and 6.11 are valid. Using the extrapolated values of $\epsilon_{||}$ and $\epsilon_{\perp}$ shown in Fig. 6.12 and 6.13 and equation 6.11 we calculate the temperature variation of $\epsilon_{||h}$. The calculated dielectric constants decrease by -0.7% at 1KHz and by -0.5% at 15KHz for the temperature range in which the TGB_A phase occurs. The experimental values decrease by $\sim 2.7\%$ at 1KHz and $\sim 2.3\%$ at 15KHz. The sharper decrease seen experimentally is due to the increase in the contribution from $\epsilon_{||}$, as the homeotropically aligned area increases at lower temperatures.

In cells treated for both homeotropic and homogeneous alignment the transi-

tions from TGB_A phase to $UTGB_{C^*}$ phase and from $UTGB_{C^*}$ phase to smectic C* phase are clearly seen (see Fig. 6.7-6.11). The tilt angle increases from zero to $\sim 10^o$ in the $UTGB_{C^*}$ phase as the temperature is decreased below the TGB_A-$UTGB_{C^*}$ transition point.

In the homogeneous geometry a square grid pattern is observed under a polarising microscope in the $UTGB_{C^*}$ phase. The structure within the $UTGB_{C^*}$ blocks is similar to that in the Smectic C* phase. Hence using equation 6.12 and the extrapolated values of $\epsilon_{||}$ and $\epsilon_{\perp}$ shown in Fig. 6.12 and 6.13 we calculate the temperature variation of $\epsilon_{\perp h}$ which is also shown in Fig. 6.17. The calculated dielectric constant ($\epsilon_{\perp h}$) increases by 0.5-0.6% at both 1KHz and 15KHz with decrease of temperature. The measured dielectric constant increases (-0.1%) at 1KHz (see Fig. 6.11) while it has a slight decrease (-0.04%) at 15KHz (see Fig. 6.9) and a sharper decrease (-0.3%) at 224KHz (Fig. 6.10). The trends at 15KHz and 224KHz are due to the relaxation of $\epsilon_{||}$ seen in Fig. 6.15 (f_d is around 15KHz at -62°C). This clearly indicates that the contribution from $\epsilon_{||}$ is much higher in the $UTGB_{C^*}$ phase compared to the other phases. The tilted molecules precess at a constant rate in the smectic C* phase about the smectic layer normal which may not be the case in the $UTGB_{C^*}$ phase. This can in turn increase the contribution from $\epsilon_{||}$ in the $UTGB_{C^*}$ phase. The detailed structure of the grain boundary region may also contribute to this result.

For homeotropic boundary condition, there is a coexistence region of homeotropically aligned unwound $UTGB_{C^*}$ domains (which mimic smectic C* domains) and $UTGB_{C^*}$ filaments with an undulatory structure. As in the case of TGB_A, even in this phase the contributions from $\epsilon_{||}$ and $\epsilon_{\perp}$ depend on the number of filaments and the alignment of the director within the filaments. The homeotropically aligned smectic C* domains widen with decreasing temperature. Within the domains as the

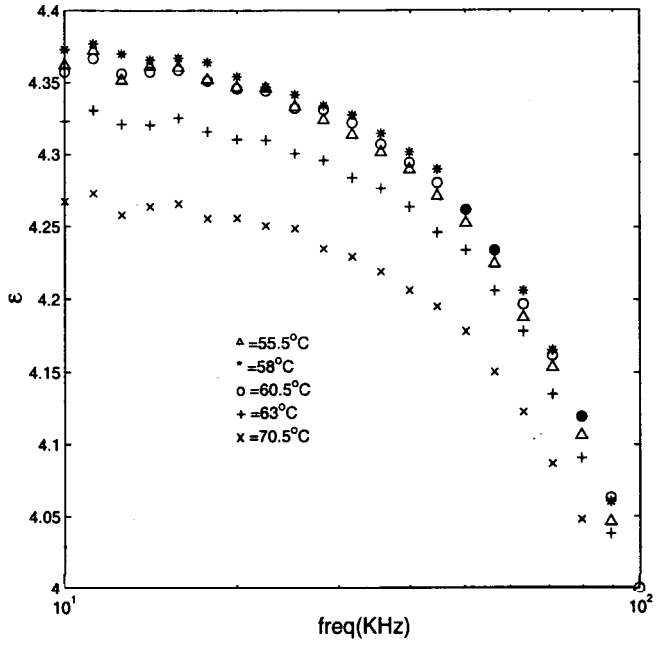

Fig. 6.18: Real part of the dielectric constant as a function of frequency for a cell treated for homogeneous alignment.

---

tilt angle increases the dielectric constant can be expected to increase. On the other hand as the number of filaments decrease with decrease of temperature, the dielectric constant can be expected to decrease. Experimentally at 1KHz the dielectric constant slightly increases ($\sim$0.1%) with decrease of temperature (Fig. 6.8). On the other hand we see a sharp decrease ($-$7%) at 15Khz (see Fig. 6.7). As discussed above this sharp decrease at 15Khz is due to the relaxation of $\epsilon_{||}$ around 15KHz, and is also reflected in Fig. 6.15. We see that the frequency dependent curves for the temperatures 62°C and 64°C are quite close, while the curves for 57.9°C and 59.9°C are well separated. This is due to the decrease of relaxation frequency with decrease in temperature.

The real and imaginary parts of the dielectric constant have been measured as functions of frequency for both the geometries (see Fig. 6.15, 6.16 and 6.18). As mentioned before, beyond 200KHz the impedance of the ITO layers is no longer

negligible and it starts contributing to the measured dielectric loss. As such, we do not present the data beyond 100KHz. In Fig. 6.18 (homogeneous alignment) the bottom most dispersion curve corresponds to the highest temperature. A reverse trend is seen in Fig. 6.15 (homeotropic alignment). In the homogeneous geometry $\epsilon_\perp$ contributes more than $\epsilon_{||}$ and vice versa in the case of homeotropic geometry. From equations 6.24 and 6.25 we can see that $\epsilon_\perp$ should increase and $\epsilon_{||}$ should decrease as the temperature is decreased for a negative dielectric anisotropy material. Hence the reverse trends with temperature seen in the two geometries can be understood.

In the homeotropic geometry we see a low frequency relaxation in all the phases. (Fig. 6.15 and 6.16). The relaxation seen in this geometry is hence due to a molecular motion and not due to a coliective mode like the Goldstone mode. The component 7(CN)5 of the binary mixture has a cyano group making a large angle ($\sim 68^o$) with the long axis of the molecule, but with a reasonably large dipole component along the long axis (see Fig. 6.6). It also has an ester group along the long axis of the molecule. The effective dipole of the ester group is opposite to the dipole component from the cyano group. Hence the net dipole moment along the long axis of the molecule is only ~ 0.25 Debye. The other compound CE8 also has an ester group along the long axis of the molecule (see Fig. 6.6) with a net component of ~ 1.4 Debye. Hence the relaxation is mainly due to the dipolar reorientation of the CE8 molecules about their short molecular axes.

In the homogeneous geometry the dielectric dispersion curve in the $UTGB_C^*$ phase is slightly above the curve corresponding to that in the smectic C* phase at 55^oC (see Fig. 6.18). This trend is clearly seen in Fig. 6.10 at 224KHz and is again due to the relaxation of $\epsilon_{||}$ seen in Fig. 6.15. This indicates that in this geometry the contribution from $\epsilon_{||}$ is much more in the $UTGB_C^*$ phase compared to the other phases. As seen in Fig. 6.18 there is a decrease in the dielectric constant beyond

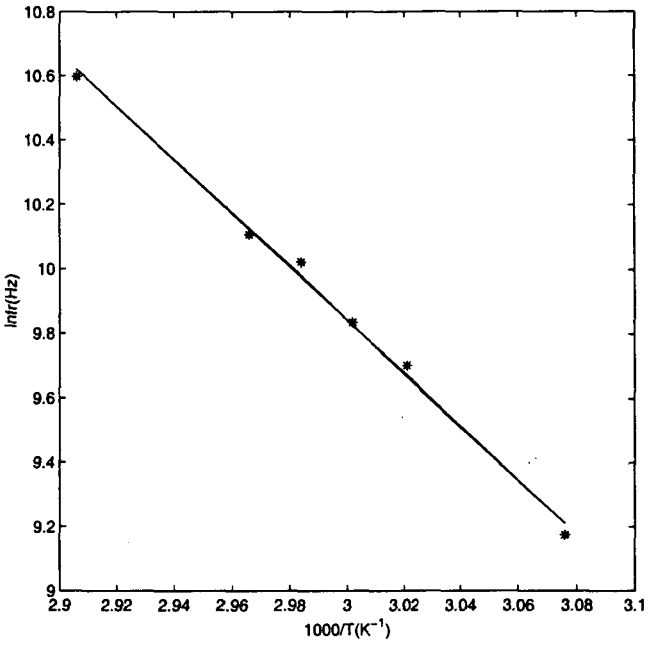

Fig. 6.19: The variation of the natural logarithm of f_d with the reciprocal of temperature in the homeotropic geometry. The continuous line is the linear fit to the experimental data.

$\sim$60KHz. There is a small contribution from $\epsilon_{||}$ even in this geometry in the UTGB$_C$* and smectic C* phases. 'Hence in both these phases due to the relaxation of $\epsilon_{||}$ the dielectric constant can show a slight decrease. We expect a Goldstone mode in the smectic C* phase in this geometry which was not observed. This may be related to the low polarisation of the compound. The polarisation has not been measured for the mixture, but that of the chiral component CE8 is only $\sim$ 4nC/cm^2 [70].

In both the geometries the imaginary parts of the dielectric constant show an increase as the frequency is decreased below $\sim$3KHz (see Fig. 6.16). This increase arises from the ionic conductivity of the sample.

Normally relaxation frequencies are used in the Arrhenius plots. As mentioned above we could not measure the relaxation frequencies as we do not see a well defined peak in the imaginary part (see Fig. 6.16) of the dielectric constant. In order to

estimate the activation energy we plot the natural logarithm of f_d versus $(1/T)$ for the homeotropic geometry which is shown in Fig.6.19. The slope of the curve gives an estimate of E_a/k_B. We estimate the activation energy to be $\sim$0.7ev which is roughly similar to that ($\sim$0.9ev) [71] measured earlier for many liquid crystals.

6.6 Conclusions

The dielectric studies were performed on a binary mixture which exhibits a new TGB phase namely $\mathrm{UTGB}_C{}^*$ phase in addition to the usual cholesteric, TGB_A and smectic C* phases. These studies were undertaken in cells treated for both homeotropic and homogeneous alignments. In both the cases the phase transitions from TGB_A phase to the recently discovered $\mathrm{UTGB}_C{}^*$ phase and from $\mathrm{UTGB}_C{}^*$ phase to smectic C* phase are clearly seen. The dielectric measurements in the homogeneous geometry clearly indicates that the contribution from $\epsilon_{||}$ is much higher in the $\mathrm{UTGB}_C{}^*$ phase compared to the other phases.

References

[1] P. G. de Gennes and J. Prost, The Physics of Liquid Cystals, 2nd ed. (Clarendon Press Oxford, 1993).

[2] S. Chandrasekhar, Liquid Crystals, 2nd ed. (Cambridge University Press, 1992).

[3] P. M. Chaikin and T. C. Lubensky, Principles of condensed matter physics (Cambridge University Press, Great Britain, 1995).

[4] R. B. Meyer, "Piezoelectric effects in Liquid Crystals," Phys. Rev. Lett. 22, 918 (1969).

[5] P. A. Pramod, R.Pratibha, and N. V. Madhusudana, "A three-dimensionally modulated structure in a chiral smectic-C liquid crystal," Current Science 73, 761 (1997).

[6] W. H. de Jeu, Physical properties of liquid crystalline materials, 1st ed. (Gordan and Breach Science publishers, 1980).

[7] G. Vertogen and W. H. de Jeu, Thermotropic Liquid Cystals, Fundamentals, Vol. 45 of Springer Series in Chemical Physics (Springer-Verlag, New York, 1988).

[8] P. G. de Gennes, "An analogy between Superconductors and Smectics A," Solid state Commun. **10,** 753 (1972).

[9] S. R. Renn and T. C. Lubensky, "Abrikosov dislocation lattice in a model of the cholesteric-to-smectic-A transition," Phys. Rev. A **38,** 2132 (1988).

[10] A. Rapini and M. Papoular, J. Physique Colloq. 30 (1969).

[11] J. Prost and J. P. Marcerou, "On the microscopic interpretation of Flexoelectricity," J. Phys. **38,** 315 (1977).

[12] F. M. Leslie, Advances in Liquid Crystals (Academic Press, New York, 1979).

[13] W. H. Press, S. A. Teukolsky, W. T. Vellerling, and B. P. Flannery, Numerical recipes, 2nd ed. (Cambridge University Press, 1992).

[14] L. Pohl, R. Eidenschink, J. Krause, and G. Weber, "Nematic Liquid Crystals with positive dielectric and negative diamagnetic anisotropy," Phys. Lett. **65A,** 169 (1978).

[15] H. Yokoyama and H. A. van Sprang, "A novel method for determining the anchoring energy function at a nematic liquid crystal-wall interface from director distortions at high fields," J. Appl. Phys. 57, 4520 (1985).

[16] H. Yokoyama, S. Kobayashi, and H. Kamei, "Temperature dependence of the anchoring strength at a nematic liquid crystal-evaporated SiO interface," J. Appl. Phys. **61,** 4501 (1987).

[17] D.-S. Seo, Y. Iimura, and S. Kobayashi, "Temperature dependence of the polar anchoring strength of weakly rubbed polyimide films for the nematic liquid crystal (5CB)," Appl. Phys. Lett. **61,** 234 (1992).

[18] S.-T. Wu and C.-S. Wu, "Experimental confirmation of the Osipov-Terentjev theory on the viscosity of nematic liquid crystals," Phys. Rev. A 42, 2219 (1990).

[19] H. H. Graf, H. Kneppe, and F. Schneider, "Shear and rotational viscosity coefficients of two nematic liquid crystals," Mol. Phys. 77, 521 (1992).

[20] F. J. Bock, H. Kneppe, and F. Schneider, "Determination of the rotational viscosity of nematic liquid crystals over an extended range.," Liq. Cryst. **3,** 217 (1988).

[21] L. M. Blinov, *Electro-optical and Magneto-optical properties of Liquid crystals.* (Wiley New York., 1983).

[22] J. P. Marcerou and J. Prost, "The Different Aspects of Flexoelectricity in Nematic~,'Mol. Cryst. Liq. Cryst. **58,** 259 (1980).

[23] L. A. Beresnev, L. M. Blinov, S. A. Davidyan, S. G. Kononov, and S. B. Yablonskii, "Direct measurement of the flexoelectric polarization of nematic liquid crystals," JETP Lett. **45,** 755 (1987).

[24] I. Dozov, I. Penchev, Martinot-Lagarde, and G. Durand, "On the sign of Flexolelectric coefficients in Nematic Liquid Crystals," Ferroelectric Lett. **2,** 135 (1984).

[25] P. R. Maheswaramurthy, V. A. Raghunathan, and N. V. Madhusudana, "An AC electrooptic technique of comparing the two anchoring energies of a hybrid aligned nematic cell," Liq. Cryst. **14,** 1107 (1993).

[26] .P. R. Maheswaramurthy, V. A. Raghunathan, and N. V. Madhusudana, "Experimental determination of the flexoelectric coefficients of a number of nematogens," Liq. Cryst. **14,** 483 (1993).

[27] N. V. Madhusudana and V. A. Raghunathan, "Influence of flexoelectricity on electrohydrodynamic instabilities in nematics," Liq. Cryst. **5,** 1789 (1989).

[28] H. Schad and M. A. Osman, "Elastic constants and molecular association of cyano - substituted nematic liquid crystals," J. Chem. Phys. **75,** 880 (1981).

[29] M. Monkade, Martinot-Lagarde, and G. Durand, "Electric Polar Surface Instability in Nematic Liquid Crystals," Europhys. Lett. 2, 299 (1986).

[30] G. Barbero and G. Durand, "Selective ions adsorption and nonlocal anchoring energy in nematic liquid crystals," J. Appl. Phys. **67,** 2678 (1990).

[31] A. C. Diogo and A. F. Martins, "Order parameter and temperature dependence of the hydrodynamic viscosities of Nematic Liquid Crystals," Mol. Cryst. Liq. Cryst. **66,** 133 (1981).

[32] G. R. Luckhurst, in Recent Advances in Liquid *Crystalline* Polymers, L. L. Chapoy, ed., (Elsevier Applied Science Publishers Ltd, 1986).

[33] A. Buka and W. H. de Jeu, "Diamagnetism and orientational order of nematic liquid crytstals.," J. Phys. **43,** 361 (1982).

[34] I. Dozov, Martinot-Lagarde, and G. Durand, "Conformational flexoelectricity in nematic liquid crystals," J. Phys. Lett. 44 (1983).

[35] G. Basappa and N. V. Madhusudana, "Evidence for polar polar short range order," Euro. Phys. J. B **1,** 179 (1998).

[36] A. J. Leadbetter, R. M. Richardson, and C. N. Colling, "The structure of a number of nematogens," J. Phys. **36,** C1–37 (1975).

[37] F. Hardouin and A. M. Levelut, "Xray study of the reentrant polymorphism N-S_A-N-S_A in a pure liquic crystal compound.," J. Phys. **41,** 41 (1980).

[38] J. Prost and J. Toner, "Dislocation-loop melting theory of phase diagrams with nema tic regions surrounded by smectic regions.," Phys. Rev. **A36,** 5008 (1987).

[39] G. Nounesis, S. Kumar, S. Pfeiffer, R. Shashidhar, and C.W.Garland, "Experimental observation of a transition between two uniaxial nematic liquid crystal phases.," Phys. Rev. Lett. **73,** 565 (1994).

[40] P. E. Cladis, "The reentrant nematic enhanced smectic A phases and molecular composition.," Mol. Cryst. Liq. Cryst. **67,** 177 (1981).

[41] N. V. Madhusudana and J. Rajan, "A simple molecular theory of double reentrance exhibited by highly polar compounds.," Liq. Cryst 7, 31 (1990).

[42] A. S. Govind and N. V. Madhusudana., "A simple molecular theory of a nematic-nematic phase transition in highly polar compounds.," Liq. Cryst. **14,** 1539 (1393).

[43] A. S. Govind and N. V. Madhusudana., "A simple molecular theory of the SmA_1-SmA_d critical point and nematic lake in highly polar compounds.," Liq. Cryst. 23, 327 (1997).

[44] P. Barois, J. Pommier, and J. Prost, in Solitons in Liquid Crystals, L. Lam and J. Prost, eds., (Springer-Verlag, New York, 1992).

[45] A. K. Zeminder, S. Paul, and R. Paul, "Refractive indices in nematic phases," Mol. Cryst. Liq. Cryst. **61,** 191 (1980).

[46] A. Yariv and P. Yeh, Optical Waves in Crystals (Wiley New York., 1984).

[47] V. V. Titov, E. I. Kovshev, A. I. Pavluchenko, V. T. Lazareva, and M. F.Grebenkin, "Synthesis and properties of nematic liquid crystals exhibit ing a positive dielectric anisotropy.," J. Phys. **36,** C1–387 (1975).

[48] F. Beaubois and J. P. Marcerou, "Biaxial nematic and smectic-A boundaries in

thin planar samples of 80CB aligned by rubbed polyimide," Europhys. Lett. **36,** 111 (1996).

[49] H. Mada and S. Kobayashi, "Surface and bulk order parameters of a nematic liquid crystal.," Appl. Phys. Lett. **35,** 4 (1979).

[50] P. Sheng, "Boundary layer phase transition in nematic liquid crystals.," Phys. Rev. A **26,** 1610 (1982).

[51] L. D. Landau and E. M. Lifshitz, Statistical Physics, 3rd part 1 ed. (Pergamon Press, 1980).

[52] P. K. Mukherjee, T. R. Bose, D. Ghose, and M. Saha, "Inclusion of density variation in the Landau-de Gennes theory of the nematic-isotropic phase transition.," Phys. Rev. E **51,** 4570 (1995).

[53] L.Onsager, Ann. N Y Acad. Sci. **51,** 627 (1949)

[54] A. P.Kapustin and N. T.Bykova, Sov. Phys.-Crystallogr. **11,** 297 (1966).

[55] R. G. Horn and T. E. Faber, "Molecular alignment in nematic liquid crystals : a comparison between the results of experiments at high pressure and predictions based on mean field theories.," Proc. R. Soc. Lond.A. 368, 199 (1979).

[56] E. F. Gramsbergen, L. Longa, and W. H. de Jeu, "Landau theory of the nematic-isotropic phase transitions," Phys. Rep. **135,** 195 (1986).

[57] R.Alben, J. R.Mccoll, and C. S.Shih, "The characterization of order in nematic liquid crystals.," Solid State Commun. **11,** 1081 (1972).

[58] D. W. Allender and M. A.Lee, "Landau Theory of Biaxial Nematic Liquid Crystals.," Mol. Cryst. Liq. Cryst. **110, 331** (1984).

[59] R.Kiefer and G.Baur, "Molecular Biaxiality in Nematic Liquid Crystals as Studied by Infrared Dichroism," Mol.Cryst. Liq. Cryst. 174, 101 (1989).

[60] C.Vause and J.Sak, "Theory of the Landau critical point.," Phys. Rev. B **18,** 1455 (1978).

[61] C. J. F. Bo¨ttcher and P. Bordewijk, *Theory of Electric Polarisation* (Elsevier, Amsterdam, 1978).

[62] N. E. Hill, W. E. Vaughan, A. H. Price, and M. Davies, *Dielectric properties and molecular behaviour* (Van Nostrand Reinhold Company, 1969).

[63] P. Debye, *Polare Molekeln* (Hirzel Verlag,Leipzig, 1929).

[64] W. Maier and G. Meier, Z. Naturforsch **16a,** 262 (1961).

[65] J. W.Goodby, M. A.Waugh, S. M.Stein, E.Chin, R.Pindak, and J. S. Patel, "Characterisation of a new helical smectic liquid crystal.," Nature **337,** 449 (1989).

[66] H. T. Nguyen, A. Bouchta, L. navailles, P. Barois, N. R. J. Tweig, A. Maaroufi, and C. Destrade, "TGB_A 'and TGB_C phases in some chiral tolan derivatives.," J. Phys. 2, 1889 (1992).

[67] C.Girould, C.Legrand, N.Isaert, P.Pochat, J. P. Parneix, H. T. Nguyen, and C. Destrade, "Dielectric Investigation of the Helical Smectic A* (TGB_A)-S^*_C phase transition.," Ferroelectrics **147,** 171 (1993).

[68] F.Bougrioua, N.Isaert, C.Legrand, A. Bouchta, P. Barois, and H. T. Nguyen, "Dielectric Properties of TGB_A and TGB_C phases.," Ferroelectrics **180,** 35 (1996).

[69] F. Gouda and W. Kuczynski, "Determination of the dielectric biaxiality in a chiral smectic-C phase.," Phys. Rev. A 46, 951 (1992).

[70] G. Spruce and R. D. Pringle, "Measurement of spontaneous polarization in ferroelectric smectic liquid crystals.," Liq. Cryst. **3,** 507 (1988).

[71] H. Kresse, *Advances in Liquid Crystals* (Academic Press, 1983), Vol. 6.